The Influence of Lateral Spreading upon Solitary Wave Formation by Internal Tides

Kehan Li,[a] Bruce R. Sutherland,[a,b]

[a] *Department of Earth and Atmospheric Sciences, University of Alberta, Edmonton, AB, T6G 2E3, Canada*

[b] *Department of Physics, University of Alberta, Edmonton, AB, T6G 2E1, Canada*

Corresponding author: Bruce R. Sutherland, bruce.sutherland@ualberta.ca

ABSTRACT: As internal tides propagate in the ocean, they carry and dissipate energy over hundreds and even thousands of kilometers. In relatively shallow seas the low vertical mode internal tide can evolve to form solitary waves whose surface signature can be detected by satellites as regions of high and low reflectance where the surface is roughened or smoothed respectively by horizontally convergent and divergent flows induced by the waves. To gain insight into what processes lead to the observation of internal solitary waves by satellites, we perform fully nonlinear simulations in three dimensions to examine the evolution of horizontally propagating, vertical mode-1 internal tides as it depends on wave amplitude, ocean depth, and the spanwise extent of the waves. The background stratification is set up according to measurements in the South China Sea. The spanwise evolution of the 3D waves is examined in terms of the lateral spreading, radius of curvature, and sea surface signature corresponding to a threshold in the surface horizontal convergent and divergent flow. The evolution of sea surface signature compares favorably to a satellite image in the South China Sea, particularly for waves initially having spanwise extent comparable to their horizontal wavelength.

1. Introduction

Internal tides are generated when barotropic tides periodically move stratified ocean water across submarine topography (Balmforth et al. 2002). If the topography is sufficiently steep, vertically and horizontally propagating beams of internal tides are launched near the topography (e.g. Pétrélis et al. 2006). These beams can cause dramatic vertical displacements, leading to strong local turbulent mixing (e.g. Rudnick et al. 2003; Vic et al. 2019). The beams are composed of a superposition of high vertical modes that are observed to transform into low vertical mode internal tides (with vertical structure on the scale of the ocean depth) after interacting with the near-surface stratification (Martin et al. 2006). Though partially dissipated by local mixing, most of the energy in these beams is transported away from the topography by the low-mode waves, mostly by mode-1 waves (Echeverri et al. 2009). It is estimated that 74% of the internal tide energy near the Hawaiian ridge is radiated away from the generation site as low-mode waves (Klymak et al. 2006; Carter et al. 2008). In the Luzon Strait, east of the South China Sea, only 40% of the energy is radiated away, possibly due to the more complex bottom topography in the Luzon Strait (Garrett and Kunze 2007; Buijsman et al. 2010) and the westward propagating branch of the Kuroshio (Buijsman et al. 2010). Their radiated energy propagates westward across the South China Sea towards the continental shelf of China. These waves are observed to be dominated by a mode-1 signal having a combination of semi-diurnal and diurnal frequencies (Farmer et al. 2009; Johnston et al. 2013). When the forcing is stronger, the internal tides tend to steepen during their propagation to form solitary waves which are visible by the sea-surface signature in satellite images as shown, for example, in Fig. 1.

Given the challenging operating conditions in the Luzon Strait (Alford et al. 2015), in-situ observation data from the wave generation site has been notably scarce. Hence, the properties of the low-mode internal tide wave near the generation site around 122°E are not well established. Some progress has been made through numerical simulations (Simmons et al. 2011; Zhang et al. 2011) that included the complex topography between the Luzon Strait and the South China Sea. These correctly predicted the propagation speed of the internal tides and provided insight into their generation mechanisms, showing the process could be understood from linear theory. Such simulations are expensive however, in that they require high resolution over large horizontal domains.

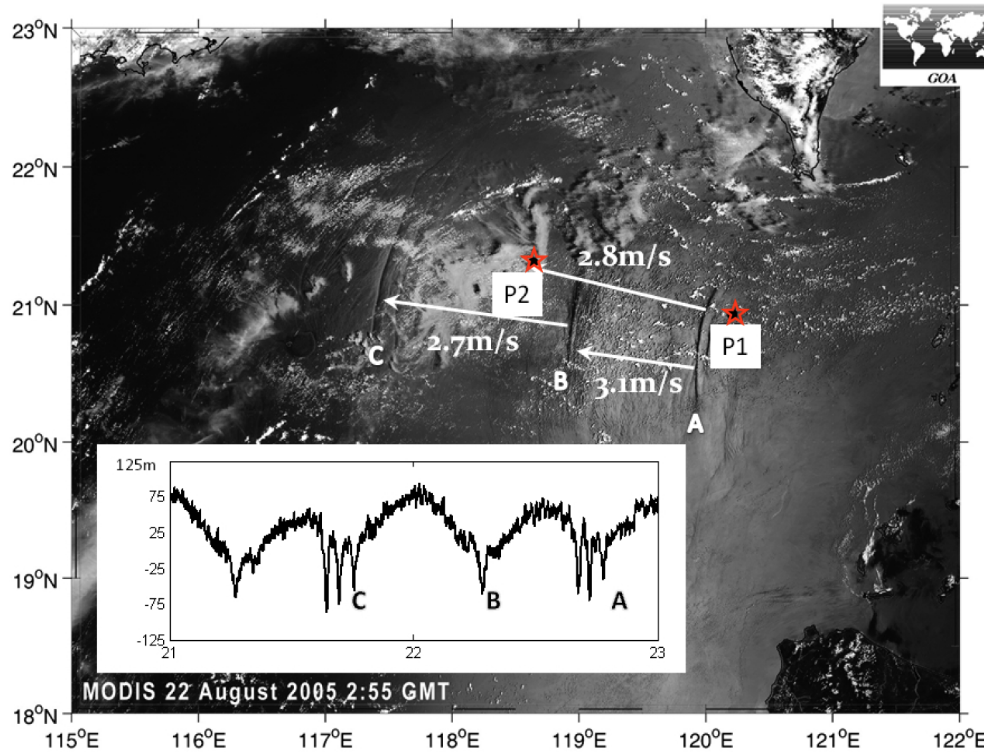

Fig. 1. MODIS image showing three nonlinear internal wave trains (labelled by A, B, and C) crossing the deep basin west of Luzon Strait. Ocean measurements were collected at the P1 and P2 locations indicated by red stars. Inset: Corresponding inverted echo-sounder time series for these waves at P2 from which path-averaged wave speeds are determined. 122°E is the estimated generation site of internal tides in the numerical models. (Image reproduced from Farmer et al. (2009).)

In general, because the internal tide has large horizontal spatial extent, on the order of a hundred kilometers, weakly nonlinear shallow water theory has been useful to diagnose circumstances leading the formation of solitary waves as it depends upon their amplitude and the strength of background rotation (Ostrovsky and Stepanyants 1989; Helfrich and Melville 2006; Helfrich and Grimshaw 2008; Grimshaw and Helfrich 2012). A different theoretical perspective on the formation of solitary waves noted that the self-interaction of the internal tide initially excites superharmonic waves with double the horizontal wavenumber (half the wavelength) (Sutherland 2016; Baker and Sutherland 2020). For sufficiently large amplitude waves with sufficiently small background rotation, the excited superharmonics may successively excite higher order superharmonics that superimpose to form solitary waves through what has been called the superharmonic cascade

(Sutherland and Dhaliwal 2022). Although the shallow water and superharmonic cascade equations are easily solved numerically, they were restricted to two dimensional internal tides having infinite spanwise extent. Thus they neglected the potentially important influence upon solitary wave formation of the spanwise spreading of laterally confined internal waves.

Extensions to shallow water theory to include the influence of lateral spreading have been explored (Karl Helfrich, pers. comm.). The approach taken here is to use numerical simulations to examine the three-dimensional evolution of spanwise-localized internal tides that disperse laterally. In this idealized study, the domain is horizontally periodic with uniform depth. Thus our results generally set criteria for the appearance of the sea-surface signature of the waves as it depends upon their initial amplitude and spanwise extent, as well as the ocean depth.

In section 2, we review the ocean measurements in the South China Sea and construct the background stratification for use in the numerical models. In addition to our simulations in three dimensions (3D), we also perform simulations in two dimensions (2D) in order to compare the evolution of spanwise finite with spanwise infinite waves. The equations for the 2D and 3D numerical models are described in section 3 along with methods used to analyze the evolution of the waves. In section 4, we present the simulation results regarding the formation of solitary wave trains as it depends on wave amplitude, the spanwise extent of the waves and ocean depth. In particular, predictions for internal solitary waves manifesting a sea surface signature is compared with satellite observations. Discussion and conclusions are presented in section 5

2. Observations and Initial Conditions

It is well-documented that solitary waves form during the evolution of westward propagating internal tides generated at Heng Chun Ridge and Lan Yu Ridge in the South China Sea Farmer et al. (2009); Li et al. (2009); Simmons et al. (2011). This inspires our interest in investigating the formation of solitary wave trains westward of this location. The observation data are taken from two separate sets of observations by Farmer et al. (2009) and Johnston et al. (2013). The dataset reported by Farmer et al. (2009) measured the full-depth stratification from 5 deployments around 21°N and 119°E during 2005 and 2007. This data is used to define approximate analytic profiles of stratification employed in our numerical simulations. The dataset reported by Johnston et al. (2013) measured the stratification around the top 300 meters of the ocean at 20.71°N and

120.45°E during UTC June 14th to July 1st 2011. This data is used to validate the structure of our approximate stratification profile near the surface.

We choose to represent the stratification by a continuous profile of the squared buoyancy frequency given by a double piecewise-exponential function of the form

$$N^2(z) = \begin{cases} N_0^2 e^{(z-z_0)/\sigma_1} & z_* \le z \le 0, \\ N_*^2 e^{(z-z_*)/\sigma_2} & -H \le z < z_*, \end{cases} \tag{1}$$

where $N^2(z_0) = N_0^2$ and $N^2(z_*) = N_0^2 e^{(z_*-z_0)/\sigma_1} = N_*^2$, such that the two exponential functions meet at $z = z_*$. Here, z_* is the depth where the stratification transitions from the upper layer to the abyssal exponential profiles and z_0 represents the depth of the surface-mixed layer. Rather than setting N^2 to zero above z_0, for simplicity, we allow the stratification to increase exponentially to the surface. Previous studies have shown that the evolution of the mode-1 internal tide is insensitive to the details of the stratification in the surface mixed layer (Sutherland and Dhaliwal 2022).

Due to noise in the observation data, it is easier to find an analytic fit to potential density profiles, $\bar{\rho}(z)$, than to $N^2(z)$. Using $N^2 = -(g/\rho_0)d\bar{\rho}/dz$ and vertically integrating Eq. (1), gives the corresponding analytic expression for potential density:

$$\bar{\rho}(z) = \begin{cases} -\frac{\rho_0 N_0^2 \sigma_1}{g}[e^{-z_0/\sigma_1}(e^{z/\sigma_1} - e^{z_*/\sigma_1})] + \rho_* & z_* \le z \le 0, \\ -\frac{\rho_0 N_0^2 \sigma_2}{g}\{e^{-(z_*/\sigma_2)-((z_0+z_*)/\sigma_1)}[e^{z/\sigma_2} - e^{-H/\sigma_2}]\} + \rho_b & -H \le z < z_*, \end{cases} \tag{2}$$

in which ρ_0 is the characteristic potential density, $\rho_\star \equiv \bar{\rho}(z_*)$ and $\rho_b \equiv \bar{\rho}(-H)$.

To construct the analytic density profiles, we set $z_0 = -30.5$ m and $z_* = -362$ m, and find the values of σ_1 and σ_2 that best fit the observations. The parameters used in this fit are listed in Table 1. The analytic potential density profile is compared with observations in Fig. 2a; the corresponding squared buoyancy frequency profile is shown in Fig. 2b.

In addition to the stratification, we prescribe other background conditions and wave properties based upon observations. These values are given in Table 2. The Coriolis parameter, f_0, was taken as a constant corresponding to a latitude of 21°N. The wave frequency, $\omega = 0.000144\,\mathrm{s}^{-1}$ was fixed, corresponding to the forcing by the M2 internal tide. Between the Luzon Strait and the observation sites, P1 and P2 (see Fig.1), of Farmer et al. (2009), the ocean depth gradually decreases from

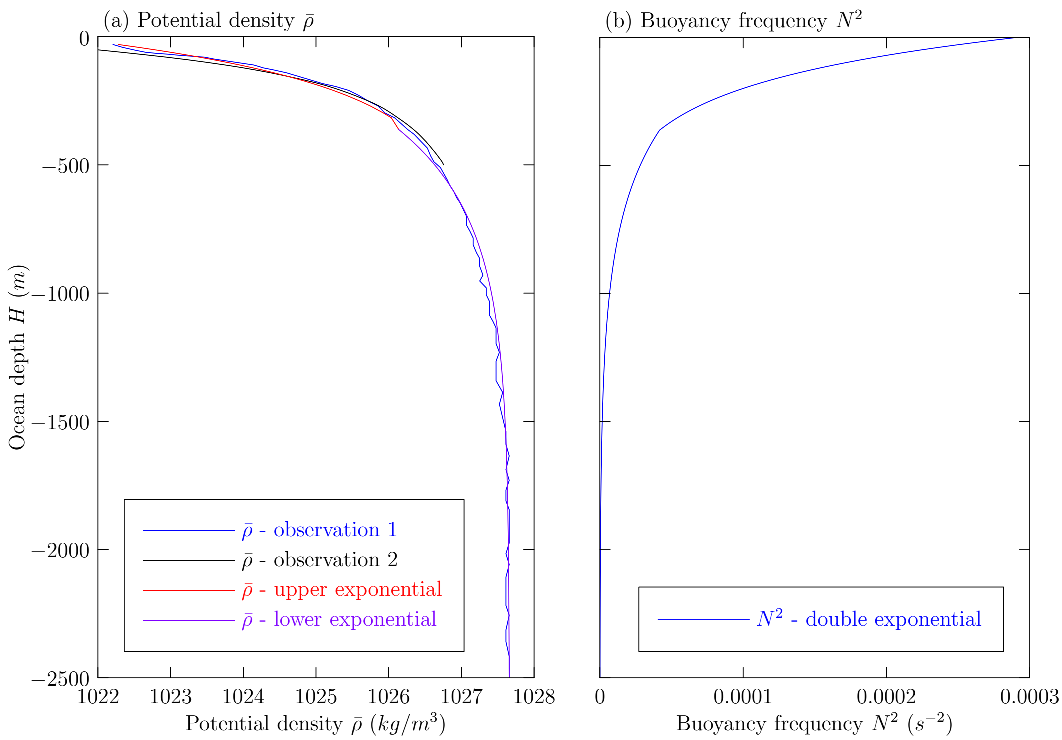

FIG. 2. (a) Comparison of the observed potential density profile to our approximation (observation 1 from Farmer et al. (2009) and observation 2 from Johnston et al. (2013)) and (b) the corresponding piecewise exponential function of squared buoyancy frequency.

Parameters	Values
ρ_0	1022.21 kg m^{-3}
ρ_*	1026.14 kg m^{-3}
ρ_b	1027.66 kg m^{-3}
z_0	−30.5 m
z_*	−362 m
N_0	0.0157 s^{-1}
N_*	0.0065 s^{-1}
σ_1	186 m
σ_2	351 m

TABLE 1. Values for the parameters that give the best-fit piecewise exponential profiles for observations of stratification in the South China Sea.

$H \simeq 3500$ m to 2000 m. Because the domain of our simulations has constant depth, we examine the influence of H on the wave evolution by running simulations at different fixed-depths in the range between 2000 and 3500 m. The maximum vertical displacement of the waves, A_0, varies

Parameters	Symbols	Values
Coriolis parameter	f_0	0.00005181 s^{-1}
Ocean depth	H	[2000-3500] m
Internal tide frequency	ω	0.000144 s^{-1}
Wavenumber	k	$[4.86\text{-}5.30]\times10^{-5}$ m^{-1}
Wavelength	λ	[119-129] km
Initial spanwise width of internal tide	σ_y	[50-125,∞] km
Initial vertical displacement amplitude	A_0	[37.5-100] m

TABLE 2. Simulation parameters governing the background values and initial structure of internal tides based upon observations in the South China Sea. The ocean depth and the internal tide wavenumber, wavelength, spanwise width and amplitude span the ranges indicated.

between the spring and neap cycles of the tide. Our simulations are initialized with horizontally periodic vertical mode-1 waves having a maximum vertical displacement amplitude in the range between 37.5 m and 100 m. Given the frequency of the waves, the horizontal wavelength, λ, (and hence wavenumber, k) varies depending upon the ocean depth H. This is found by solving the eigenvalue problem for the dispersion relation of vertical mode-1 waves in fluid of given depth, H, and determining the value of k that has frequency $\omega = 0.000144\,\mathrm{s}^{-1}$. Although there are no direct observations of the spanwise extent of the internal tide where it first develops, in our three-dimensional simulations we examine a range of widths between $\sigma_y = 50$ and 125 km to examine how the width influences lateral dispersion and the possible formation of internal solitary waves.

3. Numerical models

We performed numerical simulations in two dimensions (2D spanwise-infinite waves) and three dimensions (3D spanwise-localized waves). Both models solve the incompressible, Boussinesq equations on the f-plane in constant-depth fluid having periodic boundaries in the horizontal with free-slip upper and lower boundary conditions. In practice, the models work with non-dimensional variables, with length-related units scaled by the ocean depth H and time-related units scaled by the characteristic buoyancy frequency N_0. We begin in section 3a by describing the 2D model equations and their initial conditions. In section 3b we describe the 3D model equations. Analysis methods are described in section 3c.

a. 2D model

1) Evolution equations and numerical dissipation

We consider the evolution of 2D waves having structure in the streamwise (x) and vertical (z) directions. Although there can be motion in the spanwise (y) direction, the fields of interest are independent of y. The 2D model computed the time evolution of the spanwise vorticity, ζ, spanwise velocity, v, and buoyancy, b in the x-z plane:

$$\frac{\partial \zeta}{\partial t} = -u\frac{\partial \zeta}{\partial x} - w\frac{\partial \zeta}{\partial z} - \frac{\partial b}{\partial x} + f_0\frac{\partial v}{\partial z} + \nu\mathcal{D}\zeta, \tag{3}$$

$$\frac{\partial v}{\partial t} = -u\frac{\partial v}{\partial x} - w\frac{\partial v}{\partial z} - f_0 u + \nu\mathcal{D}v, \tag{4}$$

$$\frac{\partial b}{\partial t} = -u\frac{\partial b}{\partial x} - w\frac{\partial b}{\partial z} - N^2 w + \kappa\mathcal{D}b, \tag{5}$$

in which u, v, and w are velocities in the x, y, and z directions, respectively. In practice the equations were recast into non-dimensional variables using the length scale H (the domain depth) and time scale N_0^{-1}, in which $N_0 = 0.0157\,\mathrm{s}^{-1}$ is the characteristic buoyancy frequency (see Table 1). The results present here, however, are given in dimensional form.

The domain was discretized on an evenly spaced grid in the z-direction and in terms of their horizontal Fourier components in the x-direction (spectral representation). The spatial resolution typically consisted of 257 vertical levels and 1024 horizontal Fourier components, corresponding to 257×2049 grid points in real space. Various resolutions were tested and it was found that doubling the resolution in both directions did not quantitatively influence the results.

Although we treat the motion to be inviscid and non-diffusive, for numerical stability we include effective diffusivity in the last term on the right-hand sides of Eqs. (3) - (5). Here $\nu = 10^{-5}H^2N_0$ represents the kinematic viscosity and $\kappa = 10^{-5}H^2N_0$ represents the diffusivity. Although these numbers were much larger than realistic values for the ocean, viscous and diffusive damping was only applied to small-scale disturbances and not motion on the scale of the waves. Explicitly, the diffusion operator, $\mathcal{D}$, is a Laplacian operator acting only upon horizontal Fourier components with horizontal wavenumber greater than a cut-off wavenumber, $n_c k$, where k is the prescribed horizontal wavenumber of the parent internal tide. We typically used a cut-off of $n_c = 128$.

2) Initialization

The background stratification was set by the piecewise exponential function described in section 2. The simulations were initialized with between $n_w = 1$ and 4 wavelengths of a horizontally periodic, vertical mode-1 "parent" internal wave with a prescribed horizontal wavenumber k and vertical displacement amplitude A_0. Explicitly, the initial fields were given by

$$\zeta(x,z,0) = \frac{1}{2}\omega k \frac{N^2 - f_0^2}{\omega^2 - f^2} A_0 \hat{\psi}(z) e^{\mathrm{i}kx} + \mathrm{c.c.}, \tag{6}$$

$$v(x,z,0) = \frac{1}{2}\frac{f_0}{k} A_0 \mathrm{i}\hat{\psi}'(z) e^{\mathrm{i}kx} + \mathrm{c.c.}, \tag{7}$$

$$b(x,z,0) = \frac{1}{2} N^2(z) A_0 \hat{\psi}(z) e^{\mathrm{i}kx} + \mathrm{c.c.}, \tag{8}$$

in which c.c. denotes the complex conjugate, $\hat{\psi}(z)$ is the vertical structure of the streamfunction and $\hat{\psi}'$ is its derivative. The vertical structure function is given by the solution of the eigenvalue problem

$$\hat{\psi}'' + k^2 \frac{N^2 - \omega^2}{\omega^2 - f^2} \hat{\psi} = 0, \;\; \hat{\psi}(-H) = \hat{\psi}(0) = 0, \tag{9}$$

where $\hat{\psi}''$ denotes the second-order derivative of $\hat{\psi}$, and N^2 is given by Eq. (1). For given k, the eigenvalue problem was solved using a Galerkin method (Sutherland 2016; Baker and Sutherland 2020). From this we extract the vertical structure and the corresponding wave frequency, $\omega(k)$, of the lowest vertical mode.

3) Time-stepping

For time-stepping, an Euler forward scheme was used for diffusive terms for numerical stability, and a leapfrog scheme was employed to advance in time the non-diffusive terms:

$$\zeta(x,z,t+\Delta t) = \zeta(x,z,t-\Delta t) + 2\Delta t \dot{\zeta}, \tag{10}$$

where $\dot{\zeta}$ is the time derivative of ζ given by right-hand side of Eq. (3) without the diffusive term and Δt is the time step. Likewise, this scheme was used for the b and v fields. One loop of the leapfrog scheme involved $n_e = 20$ small time steps of $\Delta t = 0.05 N_0^{-1} \simeq 3.2$ s. So time was advanced by $1\times N_0^{-1}$ after each loop. To avoid splitting errors, the last time step in each loop was obtained by averaging the fields from the leapfrog steps at $n_e\Delta t$ and the field found from taking an Euler backstep by Δt from the field at step $(n_e+1)\Delta t$. Simulations performed with half Δt resulted in no significant quantitative differences.

b. 3D model

1) Evolution equations

The 3D model more realistically simulated the evolution of internal tides by considering the influence of waves having finite spanwise extent. Such waves will spread laterally even as the waves possibly steepen to form solitary waves. Similar to the 2D model, the 3D model used a rectangular domain with horizontally (x and y) periodic boundary conditions and free-slip upper and lower boundary conditions. The model computed the time evolution of u and v velocities in the x and y direction, respectively, and evolved the vertical displacement field, ξ, which is related to the perturbation density, ρ, by $\xi = -\rho/(d\bar{\rho}/dz)$. The equations for horizontal momentum and internal energy, neglecting viscosity and diffusion, are

$$\frac{\partial u}{\partial t} = -\frac{\partial u^2}{\partial x} - \frac{\partial vu}{\partial y} - \frac{\partial wu}{\partial z} + f_0 v - \frac{1}{\rho_0}\frac{\partial p}{\partial x}, \tag{11}$$

$$\frac{\partial v}{\partial t} = -\frac{\partial uv}{\partial x} - \frac{\partial v^2}{\partial y} - \frac{\partial wv}{\partial z} - f_0 u - \frac{1}{\rho_0}\frac{\partial p}{\partial y}, \tag{12}$$

$$\frac{\partial \xi}{\partial t} = -\frac{\partial u\xi}{\partial x} - \frac{\partial v\xi}{\partial y} - \frac{\partial w\xi}{\partial z} + w. \tag{13}$$

A diagnostic equation for vertical velocity, w, is given using incompressibility:

$$\frac{\partial w}{\partial z} = -\frac{\partial u}{\partial x} - \frac{\partial v}{\partial y}. \tag{14}$$

A diagnostic equation for the dynamic pressure, p, is found by taking the divergence of the 3D momentum equations and using incompressibility:

$$\begin{aligned}\frac{1}{\rho_0}\nabla^2 p = &-\left[\frac{\partial^2\left(u^2\right)}{\partial x^2}+\frac{\partial^2\left(v^2\right)}{\partial y^2}+\frac{\partial^2\left(w^2\right)}{\partial z^2}\right]-2\left[\frac{\partial^2(uv)}{\partial x\partial y}+\frac{\partial^2(uw)}{\partial x\partial z}+\frac{\partial^2(vw)}{\partial y\partial z}\right]\\ &+f_0\frac{\partial v}{\partial x}-f_0\frac{\partial u}{\partial y}-N^2\frac{\partial\xi}{\partial z}.\end{aligned} \tag{15}$$

A spectral representation was used for the horizontal fields, being decomposed into their Fourier components in the x and y directions. The vertical fields were decomposed into Fourier cosine series for u and v and Fourier sine series for ξ. For example, the vertical structure of ξ is represented by the sine-series coefficients, ξ_n, such that the amplitude in z is given by

$$\hat{\xi}(z)=\sum_{j=1}^{n_z}\xi_j\sin(m_j z),\quad m_j=j(\pi/H)\quad\text{and}\quad j=1,2,\ldots n_z, \tag{16}$$

in which n_z is the number of vertical modes.

The spatial domain was of size $L_x\times L_y\times H$. The streamwise extent was set by $L_x=2\pi n_w/k$, in which n_w is the initial number of horizontal wavelengths of the internal tide in the domain. The spanwise dimension was set to be $L_y=500H$ or $1000H$ depending on the initial spanwise half-width, σ_y of the waves. L_y was chosen to be at least ten times $2\sigma_y$. Typically, $n_x=512$ and $n_z=256$ grid points were used in the streamwise and vertical dimensions, respectively. Depending on the spanwise width of the waves, $n_y=256$ or 512 modes were used in the spanwise direction.

2) Exponential filter

Equations (11) - (13) do not include Laplacian diffusion for numerical stability. Because numerical noise in the 3D model grew faster compared to the 2D models, we instead applied an exponential filter to Eqs. (11), (12), and (13) at every time step. In this approach, the Fourier components with wavenumber higher than a specific cut-off wavenumber, $n_{\text{cut}}k$, were damped exponentially with increasing wavenumber (Subich et al. 2013). Taking Fourier components in the x direction as an example, a Fourier field f_n was filtered by $f_n \rightarrow \chi f_n$, in which

$$\chi(n) = \begin{cases} 1, & n < n_{\text{cut}}, \\ \exp\left[-e_1\left(\frac{n-n_{\text{cut}}}{n_{\text{mx}}-n_{\text{cut}}}\right)^{e_2}\right], & n \geqslant n_{\text{cut}}. \end{cases} \tag{17}$$

Here e_1 is the filter strength, e_2 is the filter order, and $n_{\text{mx}} \equiv n_x/2 = 256$ is the total number of Fourier components in x. We used the default values provided in Subich et al. (2013): $n_{\text{cut}} = 0.6 n_{\text{mx}}$, $e_1 = 20$, and $e_2 = 2$. Using this filter, numerical noise was damped effectively without affecting the wavenumbers having non-negligible amplitude.

3) Initialization and time-stepping

The background stratification profile was identical to the 2D model, constructed by the piecewise exponential function described in section 2. A "parent" vertical mode-1 internal tide with a prescribed horizontal wave number k and maximum vertical displacement amplitude A_0 was initialized in the domain at $t = 0$. The parent wave was a plane wave in the x direction with amplitude decaying as a Gaussian in the y-direction centered at $y = 0$. Explicitly, the three evolution equations at $t = 0$ are given by

$$\xi(x,y,z,0) = \frac{1}{2} A_0 e^{-y^2/(2\sigma_y^2)} \hat{\psi}(z) e^{\mathrm{i}kx} + \text{c.c.}, \tag{18}$$

$$u(x,y,z,0) = A_0 \frac{\omega}{k} e^{-y^2/(2\sigma_y^2)} \hat{\psi}'(z) e^{\mathrm{i}kx} + \text{c.c.}, \tag{19}$$

$$v(x,y,z,0) = \mathrm{i} A_0 \frac{f_0}{k} e^{-y^2/(2\sigma_y^2)} \hat{\psi}'(z) e^{\mathrm{i}kx} + \text{c.c.}, \tag{20}$$

in which σ_y is the standard deviation of the Gaussian.

Fig. 3 shows cross-sections of the initial streamwise velocity field (u) which has four wavelengths of the parent mode in the x direction. Here the parent mode wavelength is $\lambda_x = 50H$ and the spanwise (half-)width is $\sigma_y = 20H$. Where the ocean depth is $H \simeq 2500$ m, the wavelength corresponds to $\lambda_x \simeq 125$ km, consistent with satellite observations of the distance between successive solitary wave trains in the South China Sea.

The time scheme for the 3D model employed the same leapfrog method as used in the 2D model for the non-diffusive terms with steps of $\Delta t = 0.05 N_0^{-1}$ (see section 3a).

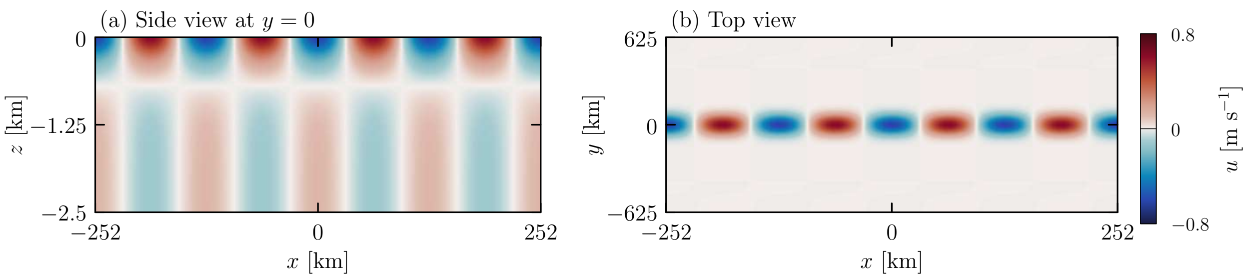

FIG. 3. Profiles of the initial streamwise velocity, u, showing (a) a vertical cross-section in the xz-plane at $y = 0$ and (b) a top view in the xy-plane at $z = 0$. Here the simulation is initialized with $n_w = 4$ wavelengths of the parent wave, $H = 2500\,\text{m}$, $A_0 = 75\,\text{m}$, $k \simeq 4.8\times10^{-5}\,\text{m}^{-1}$ and $\sigma_y = 50\,\text{km}$.

c. Analysis methods

Our focus is upon the possible development of internal solitary waves from the internal tide and how this is influenced by the ocean depth and the initial amplitude and spanwise extent of the waves. The structure of the waves was characterised in terms of the vertical displacement field, ξ, and the along-wave velocity field, u, and its x-derivative.

In 2D simulations, ξ, is given in terms of the buoyancy by $\xi = -b/N^2$; in 3D simulations, ξ is computed directly. The evolution of the displacement was examined at a depth z_m where the vertical structure of the streamfunction, and hence vertical displacement, was greatest ($\hat{\psi}(z_\text{m}) = 1$). This occurred at $z_\text{m} = -703$ m.

In 3D simulations, the spanwise extent of the waves increased due to lateral dispersion. The surface flow pattern evolved to form near-parabolic arcs and, for initial periodic waves of sufficiently large amplitude, the flow near the centerline at $y = 0$ evolved to form solitary waves. An example is shown in Fig. 4 which shows the surface streamwise velocity after 53 hours from the simulation with initial conditions shown in Fig. 3. The narrowing of regions where the streamwise velocity is large is indicative of solitary wave formation. We employ several diagnostics to characterise the spread and steepening of the waves, as described below.

The spanwise spreading of the waves was characterized in two ways. From snapshots of u at the surface, we determined the location of the wave edge, y_max, defined to be the spanwise distance from $y = 0$ where the magnitude of the peak surface streamwise velocity is no larger than is 1% of the peak streamwise velocity at $y = 0$. For example, this is indicated by the black-dashed line in

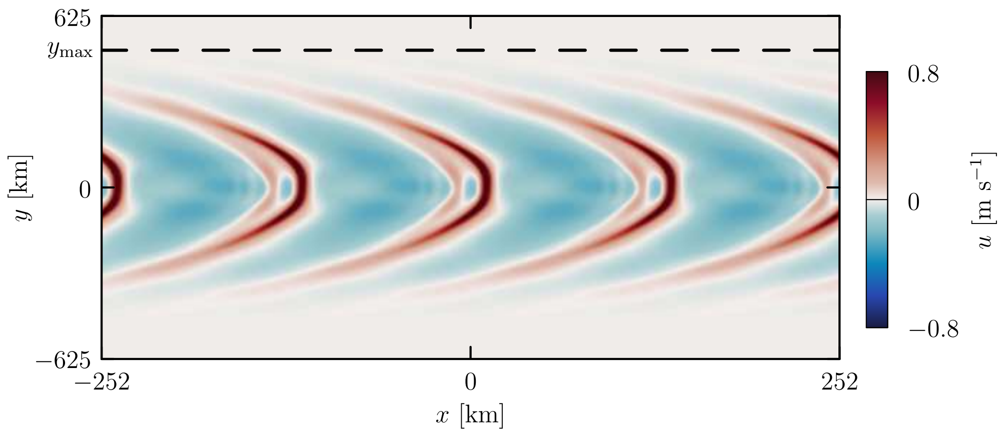

FIG. 4. Top view of u at the surface after 53 hours from the simulation with initial conditions shown in Fig. 3. The black-dashed line indicates the lateral extent of the waves, $y_{\max}$, at this time.

Fig. 4. By applying this diagnostic at successive times, we characterised the widening of the beam in time by $y_{\max}(t)$.

We also developed a diagnostic for the spanwise extent of the waves that could be compared with satellite observations of the sea-surface signature of internal solitary waves (e.g. see Fig. 1). The bright-banded surface signatures are caused by horizontally convergent flow making the surface rougher whereas darker regions are associated with horizontally divergent flow and a smoother surface. Alpers (1985) estimated that, for surface current gradients to be visible as surface roughening by satellites, their magnitudes should lie in the range $10^{-4} - 10^{-3}\,\mathrm{s}^{-1}$. In our diagnostic, we compute the x-divergent flow field, $\partial u/\partial x$, and measure where its magnitude exceeds a threshold $(\partial u/\partial x)_c = 2\times 10^{-4}\,\mathrm{s}^{-1}$. We denote by y_s the maximum spanwise distance from the centerline beyond which this threshold condition is not met. In all our simulations, $y_s(t=0)=0$ meaning that there would be no sea-surface signature of the initially periodic waves. However, a sea-surface signature can develop ($y_s > 0$) if the initial waves have sufficiently large amplitude and spanwise width to form solitary waves.

We likewise used measurements of $\partial u/\partial x$ at the surface to characterize the bending of phase lines, as shown in Fig. 5. As the waves propagated in the x direction, the contours where $\partial u/\partial x = 0$ bent to form a near-parabolic arc about $y=0$ at late times. We characterized this deformation at each time by fitting the contour to a parabola of the form $x = ay^2 + x_0$. Our results were then cast

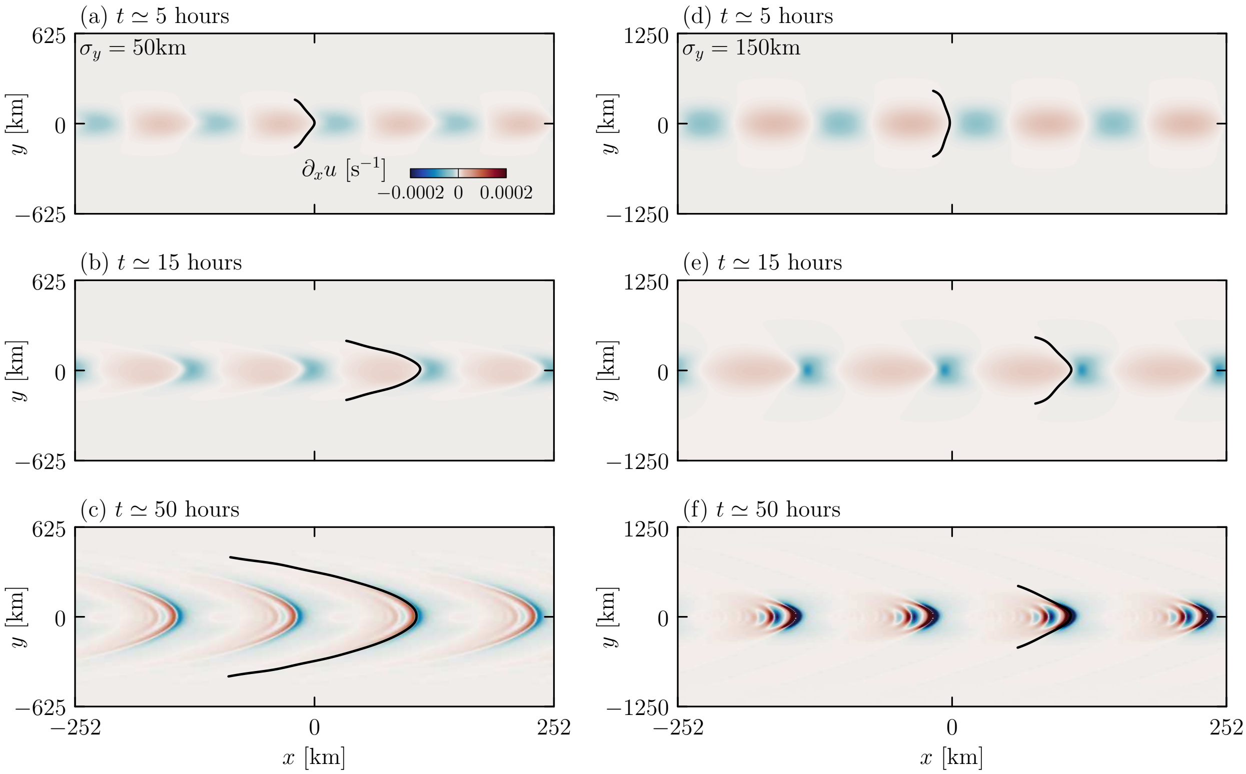

FIG. 5. Surface velocity streamwise gradient, $\partial u/\partial x$, in simulations with initially narrow and wide waves shown at three times (a,b) 5 hours, (c,d) 15 hours and (e,f) 50 hours. The simulation in (a-c) with $\sigma_y = 50$ km has initial conditions shown in Fig. 3. The simulation in (d-f) has the same initial conditions except that $\sigma_y = 150$ km and the domain has twice the spanwise extent. In each plot the superimposed black contour indicates the phase line associated with one of the four solitary waves where $\partial u/\partial x = 0$ extending laterally to $y_{\max}$. The colour scale for all plots is indicated in (a).

in terms of the radius of curvature, $R_c = 1/(2a)$. Initially R_c is infinite. And so this analysis is performed only for simulation times after 5 hours.

4. Results

Here we present simulation results examining the evolution of waves as it depends on H, A_0 and σ_y. Although the simulations were performed with nondimensional parameters based on depth scale, H, and time scale, N_0^{-1}, the results here are given in dimensional units relevant to observations in the South China Sea. In all cases the background stratification N^2 was set by the piecewise

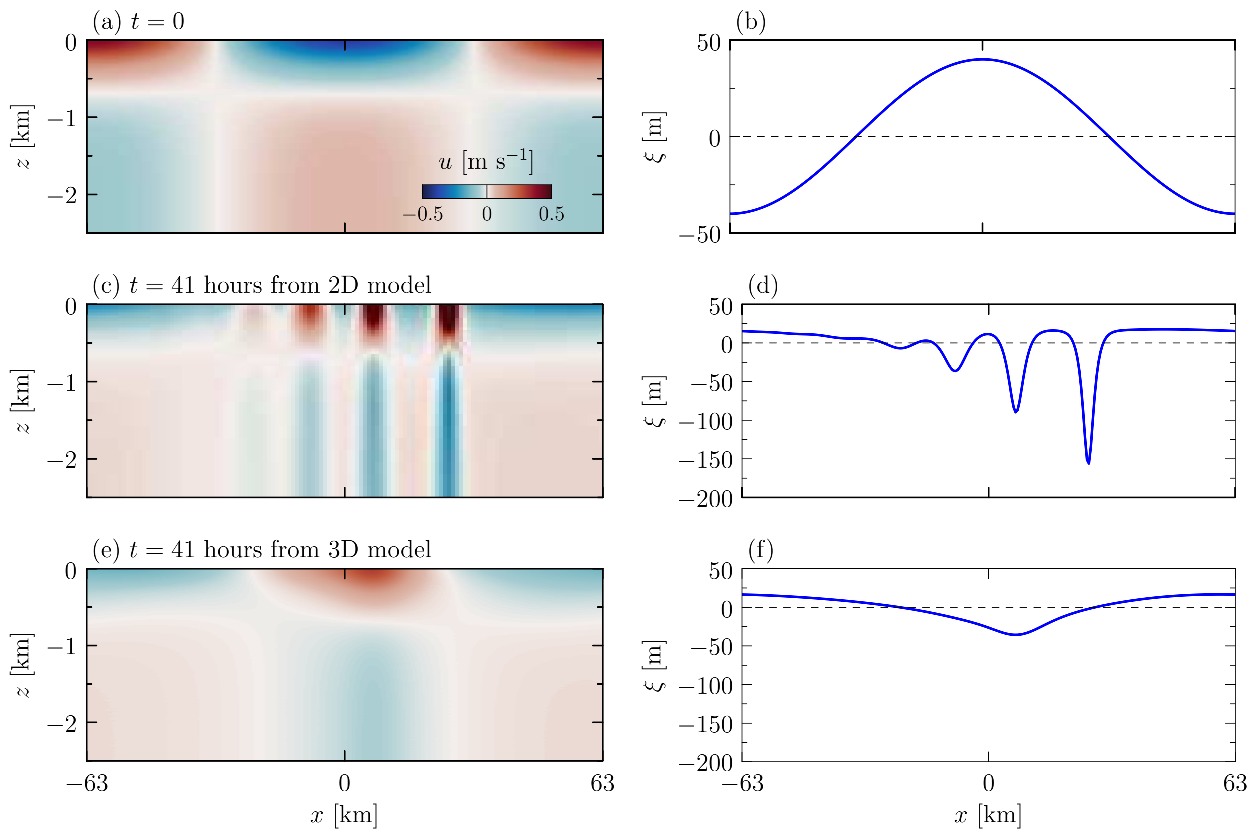

Fig. 6. Comparison of 2D and 3D simulations showing (a,c,e) vertical cross-sections of streamwise velocity at $y = 0$ and (b,d,f) vertical displacement at $y = 0$ and $z_m = -703$ m. Initial conditions, shown in (a,b) are the same for the 2D and 3D simulations. The evolution at 41 hours is shown for (c,d) the 2D model and (e,f) the 3D model with $\sigma_y = 50$ km. The simulations are initialized with one wavelength of the parent wave having $A_0 = 40$ m in total depth $H = 2500$ m. The colour scale for all streamwise velocity plots is indicated in (a).

exponential (Eq. (1)) with the parameters listed in Table 1. Values of the Coriolis parameter and the wave frequency were fixed, as given in Table 2.

We begin by comparing the evolution of spanwise infinite waves in a 2D model with a 3D simulation of waves having finite spanwise extent, $\sigma_y = 50$ km. The initial condition at $y = 0$ is the same in both simulations, as shown in Fig. 6(a,b). In these simulations, only 1 wavelength of the parent wave was initialized in the domain ($n_w = 1$).

We examine the wave structure after it has evolved for 41 hours. This is the time predicted for the waves moving at their predicted horizontal group velocity, $c_{gx} \simeq 2.55$ ms^{-1}, to reach the P2 location in the South China Sea from the generation site estimated to be located at 122°E (see Fig. 1). At this

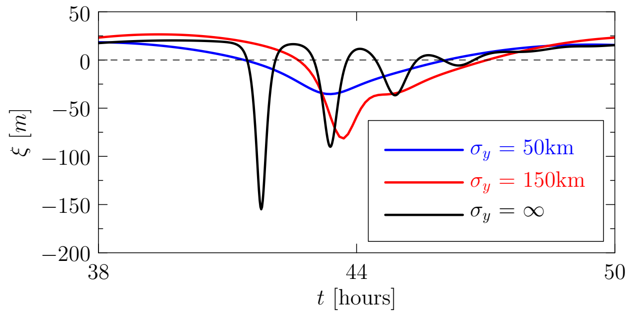

FIG. 7. Time series over one period of the initial wave of vertical displacement at $x = y = 0$ and $z = -703$ m from simulations of waves with initial spanwise width indicated in the legend. As in Fig. 6, $A_0 = 40$ m and $H = 2500$ m.

time in the 2D model, one wavelength of the periodic internal tide has evolved to form a solitary wave train containing four waves of depression with successive amplitudes decreasing toward the lee of the train (Fig. 6c,d). In contrast, the corresponding 3D simulation shows only moderate narrowing of the wave trough after 41 hours.

The degree of narrowing of the wave troughs and their maximum downward displacement becomes larger if the lateral extent of the initial waves is larger. For example, Fig. 7 plots time series of the vertical displacement at $z_m = -703$ m determined from the 2D simulation (σ_y infinite) and from 3D simulations with $\sigma_y = 50$ and 150 km. As will be shown, waves having initially smaller spanwise width spread laterally more rapidly due to dispersion. This spread of energy away from $y = 0$ reduces the centerline amplitude of the waves, inhibiting nonlinear steepening.

The strength of solitary waves, if they form, depends on the initial wave amplitude, A_0, ocean depth H, as well as the spanwise width, σ_y. Next we successively examine the influence of each of these parameters on the development of solitary waves.

Figure 8 plots time series of vertical displacement determined from six 3D simulations with different initial amplitudes. In all cases the depth is fixed at $H = 2500$ m and the initial beam width is $\sigma_y = 50$ km. As anticipated, localized solitary waves with deeper depressions become more evident as the initial amplitude increases every tidal period. Single solitary waves appear after 40 hours in simulations with $A_0 = 50$ and 62.5 m, and solitary wave trains develop at larger amplitudes. In the simulation with $A_0 = 100$ m, the solitary waves become unstable after 80 hours, at which

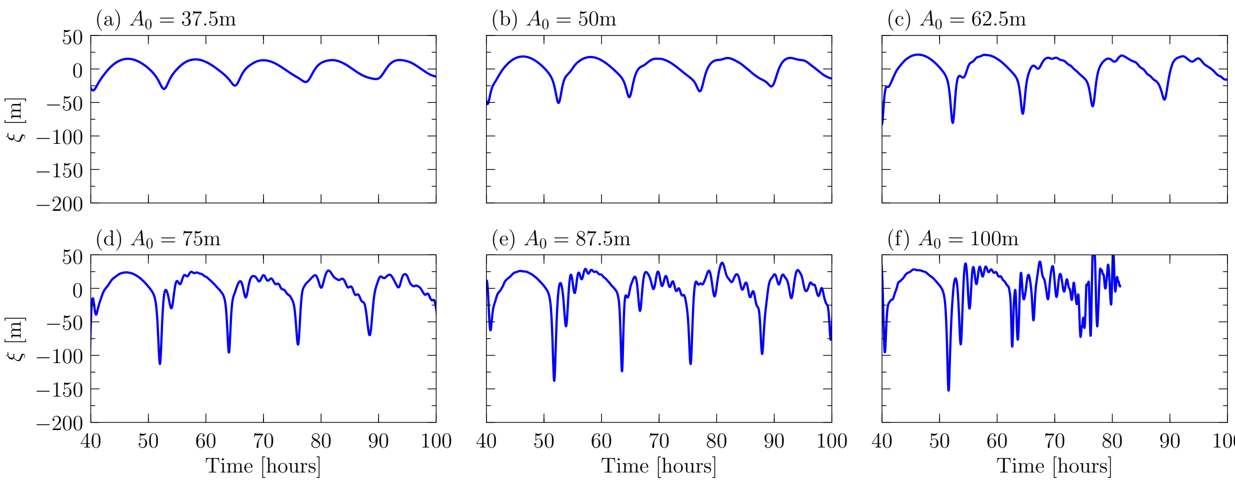

FIG. 8. Evolution of the vertical displacement over time at $x = y = 0$ and $z = -703$ m as it depends on the initial maximum vertical displacement A_0: (a) 37.5 m, (b) 50 m, (c) 62.5 m, (d) 75 m, (e) 87.5 m, and (f) 100 m. In all cases $H = 2500$ m and $\sigma_y = 50$ km.

time the simulation is terminated as it is unable to resolve the small-scale turbulent processes that result. In all cases, the maximum downward displacement, $|\xi_{\text{min}}|$, becomes larger as A_0 increases.

To investigate the dependence of solitary waves on the ocean depth in the 3D model, we ran a sequence of simulations with H ranging from 2000 m to 3500 m keeping $A_0 = 62.5$ m and $\sigma_y = 50$ km fixed. In these simulations we adjusted the initial horizontal wavenumber, k, of the waves to ensure the wave frequency, ω, was that of the semi-diurnal M_2 tide. The vertical displacement at the depth $z_m = -703$ m and for time after 40 hours are shown in Fig. 9. Qualitatively, the crests of the solitary wave trains corresponding to ξ_{max} do not significantly alter with variations in ocean depth, while the maximum downward displacement $|\xi_{\text{min}}|$ increases with increasing ocean depth. Additionally, in a greater depth domain, the crest of the solitary wave trains exhibits less small-scale oscillations, for example, at the time $t = 70 \pm 3$ hours.

To investigate the dependence of solitary waves on the initial spanwise width, we varied σ_y in the 3D model, keeping $A_0 = 62.5$ m and $H = 2500$ m fixed. The displacement for $\sigma_y = 125$ km (Fig. 10(d)) is only shown up to $t = 86$ hours, after which the waves become unstable to small-scale disturbances. As demonstrated in Fig. 10, increasing σ_y results in larger downward vertical displacements as well as small-scale oscillations along crests between successive solitary wave trains. If $\sigma_y = 125$ km, the downward peaks have a vertical displacement $\simeq -200$ m which is

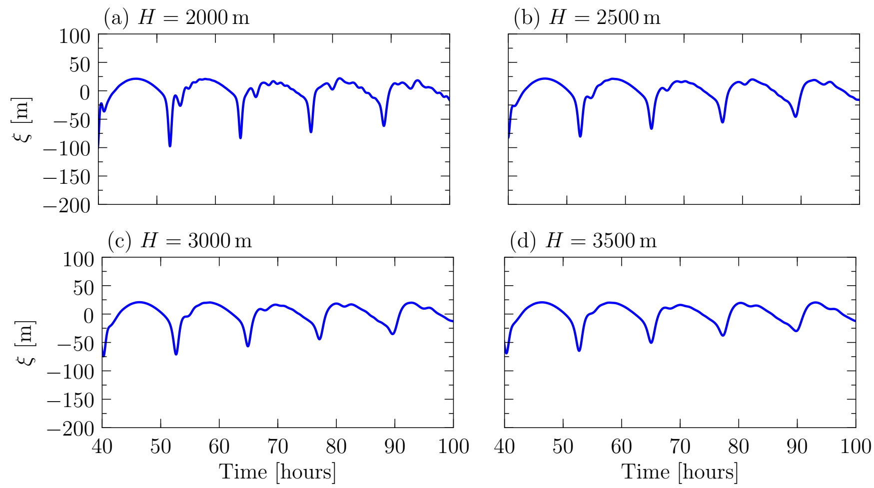

FIG. 9. As in Fig. 8, but showing the evolution of the vertical displacement as it depends on the simulated ocean depth H: (a) $H = 2000\,\mathrm{m}$ and $k \simeq 5.30\times10^{-5}\,\mathrm{m}^{-1}$, (b) $H = 2500\,\mathrm{m}$ and and $k \simeq 4.96\times10^{-5}\,\mathrm{m}^{-1}$, (c) $H = 3000\,\mathrm{m}$ and $k \simeq 4.90\times10^{-5}\,\mathrm{m}^{-1}$, and (d) $H = 3500\,\mathrm{m}$ and $k \simeq 4.86\times10^{-5}\,\mathrm{m}^{-1}$. In all cases $A_0 = 62.5\,\mathrm{m}$ and $\sigma_y = 50\,\mathrm{km}$.

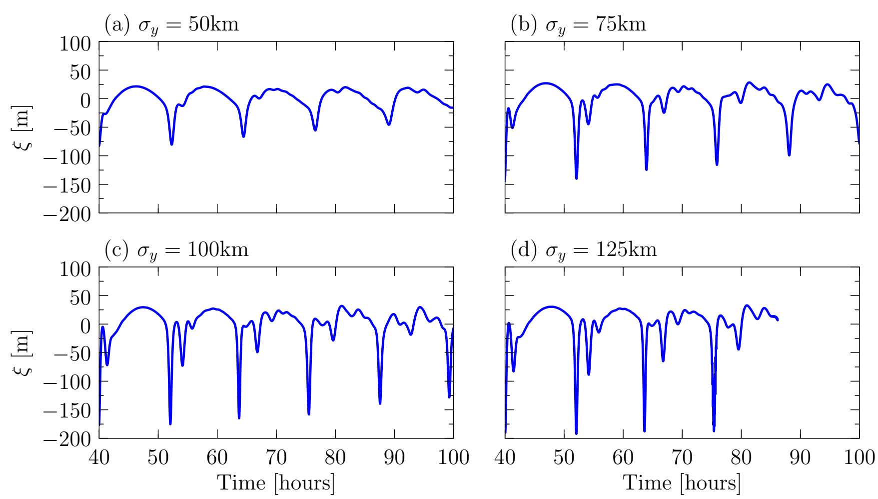

FIG. 10. As in Fig. 8, but showing vertical displacement over time as it depends on the initial spanwise width, σ_y, of the internal tide: (a) $\sigma_y = 50\,\mathrm{km}$, (b) $\sigma_y = 75\,\mathrm{km}$, (c) $\sigma_y = 100\,\mathrm{km}$, and (d) $\sigma_y = 125\,\mathrm{km}$. In all cases $H = 2500\,\mathrm{m}$ and $A_0 = 62.5\,\mathrm{m}$.

moderately less than the maximum downward displacement in the 2D simulation with similar initial wave amplitude (Fig. 8f).

Fig. 11 quantitatively summarizes the results shown in Figs. 8, 9, and 10 by plotting the dependence of the maximum descent of isopycnals, $|\xi_{\min}|$, and their maximum rise, $\xi_{\max}$, on

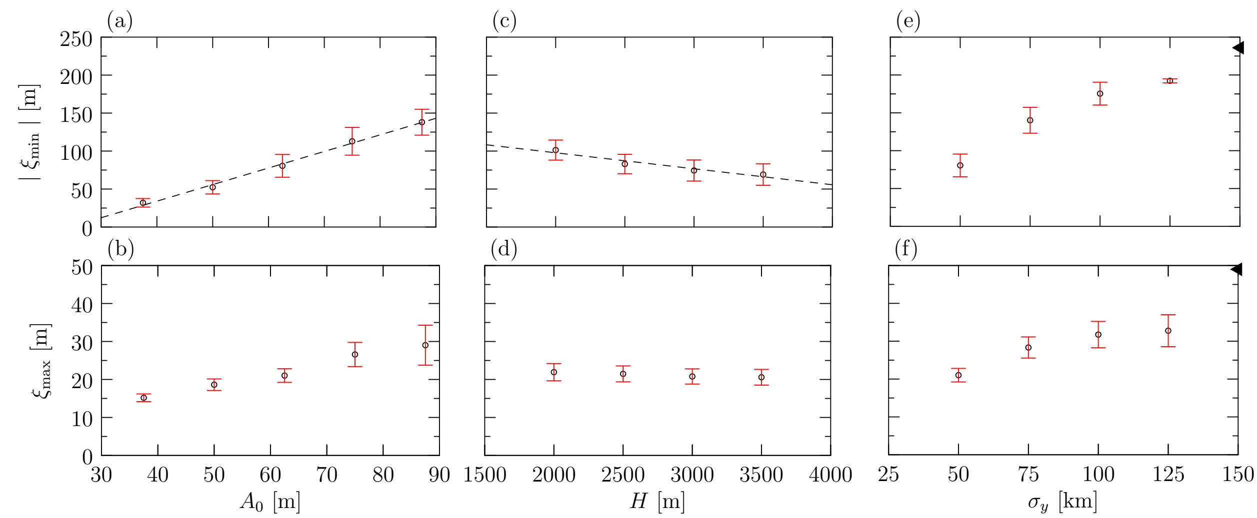

FIG. 11. Dependence of the magnitude of maximum and minimum vertical displacement on the initial wave amplitude (a,b), ocean depth (c,d), and spanwise width (e,f) from 3D simulations. Initial wave amplitude $A_0 = 75$ m in (c,d,e,f); ocean depth $H = 2500$ m in (a,b,e,f); spanwise width $\sigma_y = 50$ km in (a,b,c,d). Error bars (in red) represent the standard deviation of the four maximum and four minimum vertical displacements occurring between 40 and 90 hours. The triangles on the right side of (e,f) indicate values determined in 2D simulations ($\sigma_y \to \infty$). The dashed lines in (a,c) represent the best-fit line through the points.

the initial wave amplitude, A_0, ocean depth, H, and initial spanwise width of the waves, σ_y. At fixed H and σ_y, $|\xi_{\min}|$ increases linearly with A_0 over the range of initial amplitudes examined (Fig. 11a). In particular, for $H = 2500\,$m and $\sigma_y = 50\,$km we find $|\xi_{\min}| \simeq (2.18 \pm 0.09)\,[A_0 - (24 \pm 3)\,\text{m}]$, with A_0 measured in meters. At fixed $A_0 = 75\,$m and $\sigma_y = 50\,$km, we find the maximum descent of isopycnals decreases linearly with ocean depth (Fig. 11c) such that $|\xi_{\min}| \simeq (0.021 \pm 0.004)\,[-H + (6.7 \pm 0.6) \times 10^3\,\text{m}]$, for H measured in meters. As the spanwise width of the beam increases, so does the maximum descent of isopycnals, though its value asymptotes to 236 m for spanwise infinite waves, as determined in 2D simulations (Fig. 11e). The maximum rise of isopycnals, $\xi_{\max}$, also increases with increasing A_0, H and σ_y.

Next we examine the spanwise evolution of waves characterized by their lateral spreading at the surface, the evolution of the radius of curvature of the crescent-shaped waves, and the width of the sea surface signature as might be observed by satellite. The half-width of the laterally confined waves is characterized by $y_{\max}$, as described in Sec. 3c. Figure 12 shows that the half-width increases in time due to lateral dispersion. This spreading is insensitive to the initial amplitude of

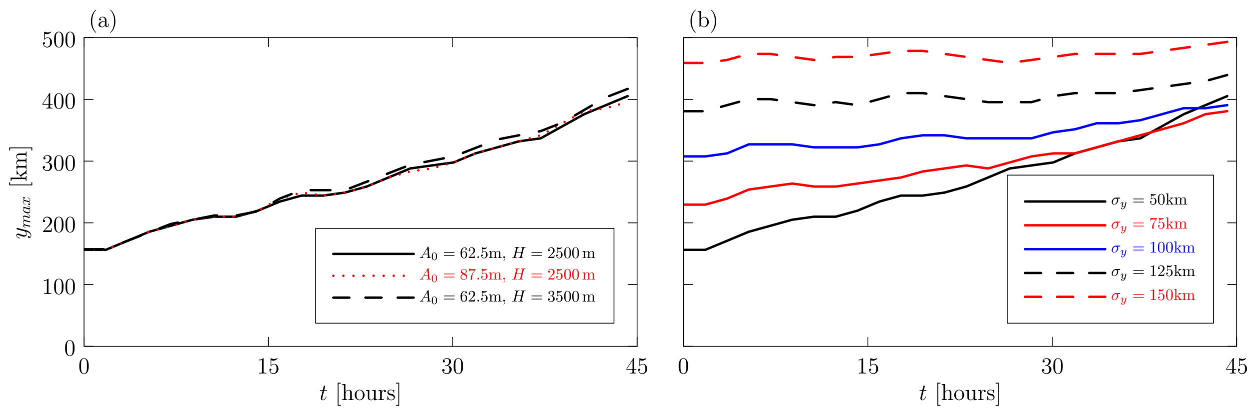

FIG. 12. Lateral extent of the waves, $y_{\max}$, over time in simulations with (a) $\sigma_y = 50$ km and different A_0 and H as indicated in the legend, and with (b) $A_0 = 62.5$ m, and $H = 2500$ m and different σ_y as indicated in the legend.

the waves, A_0, and the ocean depth, H, as evident for the three cases plotted in Fig. 12a. However, the spreading depends sensitively upon the initial spanwise extent of the waves, σ_y, increasing most rapidly if the initial width is relatively small. In the case with $\sigma_y = 50$ km, over 45 hours $y_{\max}$ more than doubles from $\simeq 156$ km to $\simeq 405$ km. In comparison, over the same time these waves are predicted to propagate 410 km at their group velocity, $c_g \simeq 2.55\,\mathrm{m\,s^{-1}}$. Hence, the lateral dispersion of such spanwise narrow internal tides is comparable with their streamwise propagation distance.

The increase in time of $y_{\max}$ is approximately linear over the first 45 hours of evolution. Finding a best-fit line to $y_{\max}$ versus time for each of the five simulations in Fig. 12(b), gives their lateral spreading rates, which are plotted in Fig. 13. The spreading rate decreases exponentially with increasing initial spanwise width, determined empirically by $\dot{y}_{\max} \simeq [17.5(\pm 3.5)\mathrm{km/hour}]\exp[-\sigma_y/(42 \pm 5\,\mathrm{km})]$.

We have seen that phase lines at the surface bend to form arcs over time, which we quantify by measuring the radius of curvature, R_c, at $y = 0$ of the zero contour associated with the $\partial_x u$ field between strongest peaks in that field (see Fig. 5). Initially phase lines are parallel to the y-axis, and their radius of curvature is infinite. Our analysis begins after 5 hours. The results showing the time evolution of R_c is shown in Fig. 14. As with the lateral spreading of the waves, we find the evolution of the curvature varies little with initial wave amplitude, A_0, and ocean depth, H, (Fig. 14a), but depends strongly on the initial spanwise extent of the waves, σ_y (Fig. 14b). If σ_y is sufficiently small ($\sigma_y \lesssim 100$ km), R_c rapidly decreases over the first 12 hours and increases

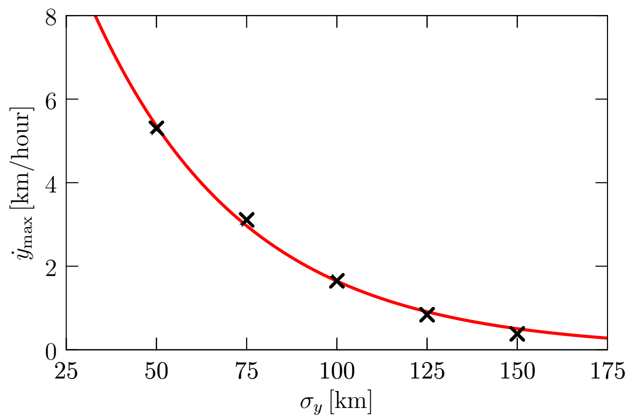

Fig. 13. Dependence of the lateral spreading rate upon initial spanwise width of the waves. The red line shows the best-fit exponential through the points.

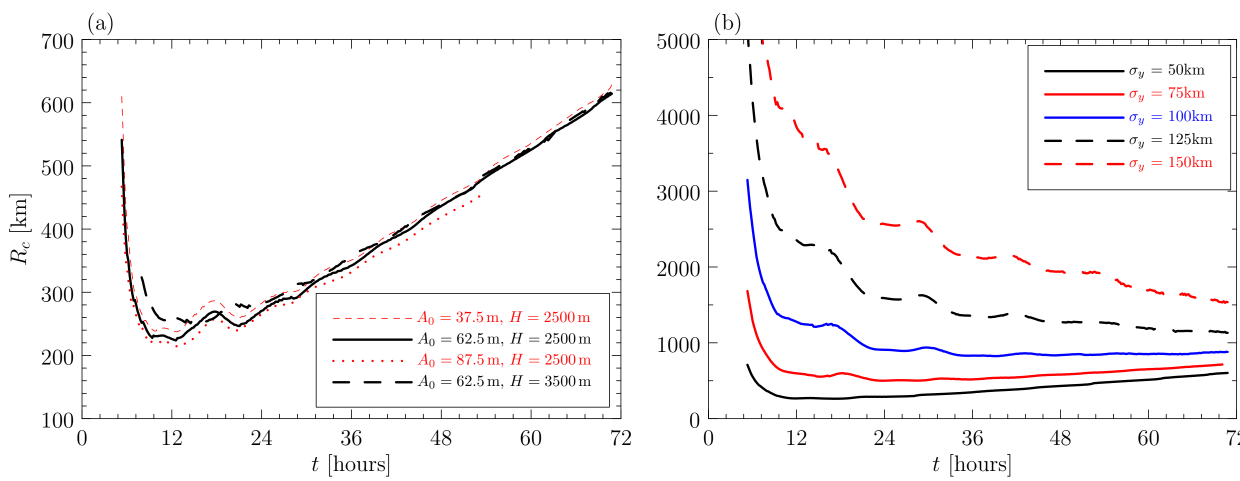

Fig. 14. Evolution of the radius of curvature, R_c, (a) with $\sigma_y = 50\,\mathrm{km}$ fixed and with different A_0 and H as indicated in the legend, and (b) $A_0 = 62.5\,\mathrm{m}$ and $H = 2500\,\mathrm{m}$ fixed and with varying σ_y as indicated in the legend.

thereafter. For simulations with $\sigma_y = 50\,\mathrm{km}$, the minimum radius of curvature is $R_c \sim 230 \pm 10\,\mathrm{km}$, which is comparable to the lateral extent, $y_{\max}$, at this time (see Fig. 12(a)). In simulations having wider initial waves ($\sigma_y \gtrsim 100\,\mathrm{km}$), the radius of curvature generally decreases over time.

At late times in all simulations, the radius of curvature is found to change approximately linearly with time. We compute this change from the slope of the best-fit line through $R_c(t)$ for times between 24 and 70 hours. The corresponding rate of change of the radius of curvature, $\dot{R}_c$, is plotted in Fig. 15. Consistent with the simulation results shown in Fig.14(b), the radius of

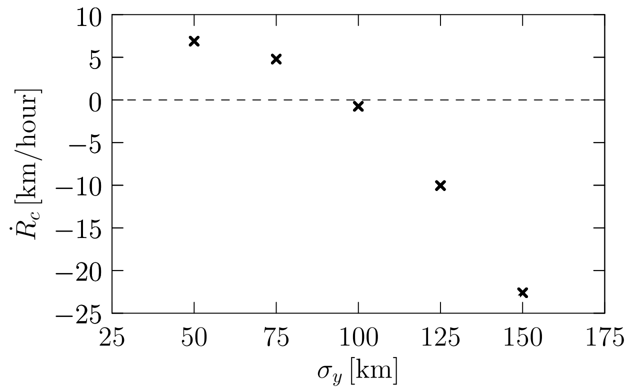

FIG. 15. From the simulations shown in Fig. 14(b), time rate of change of radius of curvature for times after 24 hours as it depends on initial spanwise extent of the waves.

curvature increases at late times if the initial spanwise extent of the internal waves is less than ~ 100 km, and it decreases otherwise. As we discuss below, satellites may observe the sea surface signature of internal tides if the waves become sufficiently steep. The analysis above suggests that successive snapshots over the course of 2 days could be used to measure the change in the radius of curvature of the sea surface signature over time from which the effective initial spanwise width of the waves could be inferred.

Satellites observe the sea surface signature of internal waves through the enhancement and reduction of the surface roughness resulting from horizontally convergent and divergent flows at the surface induced by the waves. We characterise whether or not this signature can be observed by measuring the spanwise half-width, y_s, from $y = 0$ within which the surface current gradient, $\partial u/\partial x$, exceeds a threshold value of 2.4×10^{-4} s^{-1}, as described in section 3c. For the horizontal convergence to pass the threshold, the internal tide must steepen to form solitary waves for which the horizontal flows at the surface become larger and change over smaller horizontal distances. From our previous analyses, we expect a stronger, wider and longer lasting sea surface signature in shallower domains for internal waves which initially have larger amplitude and wider horizontal extent: these more rapidly form solitary waves and, because the lateral spreading is less pronounced, the solitary waves persist for longer times.

Figure 16 plots the evolution of the half-width, y_s, in time for six simulations. In the simulation with $\sigma_y = 50$ km, $A_0 = 75$ m and $H = 2500$ m the internal waves have steepened sufficiently after $\simeq 36$ hours for a sea surface signature to be evident by satellite. However, the lateral spreading

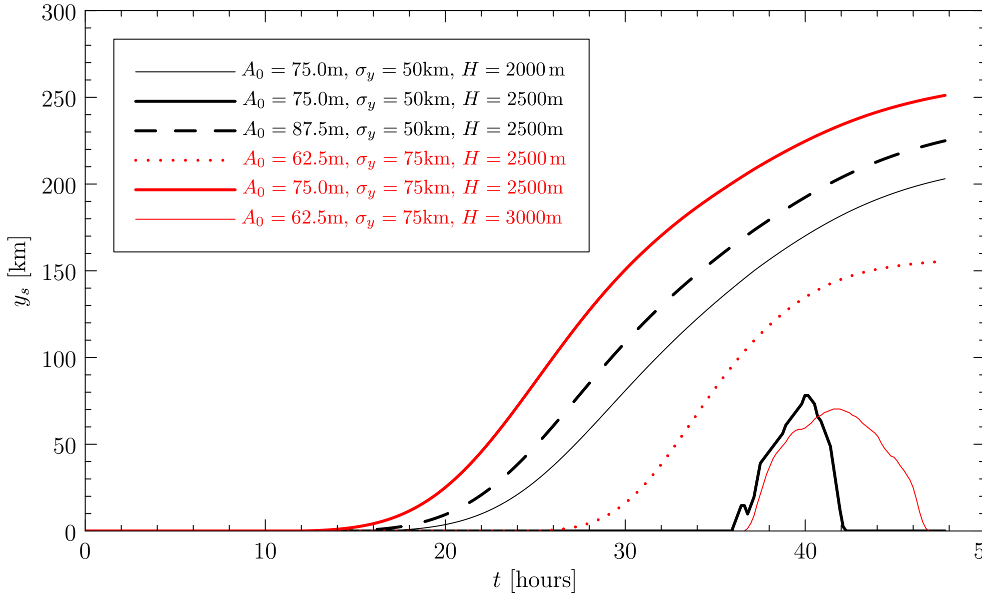

FIG. 16. Predicted width of sea surface roughness signature, y_s, over time for simulations with different initial vertical displacement amplitudes, A_0, spanwise widths, σ_y, and depths, H, as indicated.

of these relatively narrow waves results in a reduction of the wave amplitudes such that the sea surface signature disappears after $\simeq 42$ hours. For the same waves in shallower fluid ($H = 2000$ m) or with larger initial amplitude ($A_0 = 87.5$ m), the sea surface signature becomes pronounced much earlier (after $\simeq 18$ hours) and its half-width extends beyond 200 km over the following 30 hours. In simulations with greater depth ($H \gtrsim 3000$ m) or smaller amplitude waves ($A_0 \lesssim 62.5$ m) the threshold criterion for having a sea surface signature is never met. In simulations of waves having a wider horizontal extent ($\sigma_y = 75$ km), the threshold criteria is met at relatively larger H and smaller A_0. In particular, with $H = 2500$ m, a sea surface signature eventually appears after $\simeq 37$ hours for waves having initial amplitude as small as $A_0 = 62.5$ m, though their signal vanishes after $\simeq 47$ hours due to lateral spreading.

5. Discussion and conclusions

We performed fully nonlinear simulations to examine the evolution of the low-mode internal tide as it depends on wave amplitude, ocean depth, and the spanwise extent of the waves in stratification characteristic of measurements taken in the South China Sea. Solitary waves of depression were found to evolve from the initial horizontally sinusoidal internal tide provided the initial amplitude and spanwise extent of the waves were sufficiently large, with the maximum depression amplitude being more pronounced in shallower fluid. Corresponding to the deepening and narrowing of isopycnals associated with solitary waves, the horizontal flow at the surface exhibited stronger horizontal gradients which can result in enhanced sea surface roughening that can be observed by satellite. However, this manifestation of internal waves at the surface was retarded if the initial amplitude and spanwise extent of the waves were too small or the domain too deep.

For the satellite image shown in Fig. 1, internal solitary waves in the South China Sea are evident by the arc-shaped pattern of sea surface roughness at locations A, B and C. In particular, the sea surface pattern indicated by A (near the observation location P1) has half-width $\simeq 50\,\mathrm{km}$. We predict that the mode-1 internal tide originating $\simeq 200\,\mathrm{km}$ to the east at 122°E would take 22 hours to propagate to site A at the group velocity $2.55\,\mathrm{m\,s^{-1}}$, comparable with the observed speeds. The waves at A occur in an ocean depth $H \simeq 3000\,\mathrm{m}$. The sea surface signature has half-width of 46 km and a radius of curvature $\simeq 400\,\mathrm{km}$. Thus our analyses suggest the effective initial spanwise extent of the waves was $\sigma_y \simeq 75\,\mathrm{km}$ with initial maximum vertical displacement amplitude $\simeq 65\,\mathrm{m}$. For waves with $\sigma_y \simeq 75\,\mathrm{km}$, the radius of curvature is expected to increase in time $\simeq 12$ hours after generation, which is observed for the waves that have propagated from location A to locations B and C: these have less latitudinally curved sea surface signatures with $R_c \simeq 466\,\mathrm{km}$ and $R_c \simeq 472\,\mathrm{km}$, respectively.

Although this our model is able to simulate the relatively realistic evolution of internal tides, it has many simplifying assumptions. Besides assuming a stationary background, we have focused on the evolution of the vertical mode-1 internal tide in uniform-depth fluid. By assuming initially sinusoidal waves in a periodic domain, we are in effect examining the temporal evolution of the waves in a frame of reference moving at their initial group velocity. Simulations with different initial amplitudes thus examine the evolution of waves originating from different phases between the spring and neap tides. Simulations with different domain depths given insights into the influence of depth upon steepening of the waves. Generally we find that the lateral spreading and radius of curvature of the waves about their centerline do not depend significantly upon amplitude and depth, but do depend strongly on the initial lateral extent, σ_y, of the waves: the rate of spread decays exponentially with increasing σ_y; the radius of curvature after $\simeq 12$ hours increases for $\sigma_y \lesssim 100\,\mathrm{km}$ and decreases for larger σ_y.

The generic nature of these results suggests they may be applied to other regions in the ocean where internal solitary waves are observed by satellite. A complete categorization of the time evolution of the span and radius of curvature of the sea surface signature as it depends upon ocean depth and initial wave amplitude and spanwise extent could prove a useful tool in understanding the origins of internal solitary waves globally.

Acknowledgments. Funding for this research has been provided by the Natural Sciences and Engineering Research Council.

Data availability statement. The data from this study is available from the authors upon request.

References

Alford, M. H., and Coauthors, 2015: The formation and fate of internal waves in the South China Sea. *Nature*, **521**, 65–69.

Alpers, W., 1985: Theory of radar imaging of internal waves. *Nature*, **314**, 245–247.

Baker, L., and B. R. Sutherland, 2020: The evolution of superharmonics excited by internal tides in non-uniform stratification. *J. Fluid Mech.*, **891**, R1.

Balmforth, N. J., G. R. Ierley, and W. R. Young, 2002: Tidal conversion by subcritical topography. *J. Phys. Oceanogr.*, **32 (10)**, 2900–2914.

Buijsman, M., J. McWilliams, and C. Jackong, 2010: East-west asymmetry in nonlinear internal waves from Luzon Strait. *J. Geophys. Res.*, **115**, C10 057.

Carter, G. S., and Coauthors, 2008: Energetics of M2 barotropic-to-baroclinic tidal conversion at the Hawaiian Islands. *J. Phys. Oceanogr.*, **38**, 2205–2223.

Echeverri, P., M. R. Flynn, K. B. Winters, and T. Peacock, 2009: Low-mode internal tide generation by topography: An experimental and numerical investigation. *J. Fluid Mech.*, **636**, 91–108.

Farmer, D., Q. Li, and J.-H. Park, 2009: Internal wave observations in the South China Sea: The role of rotation and non-linearity. *Atmos. Ocean*, **47**, 267–280.

Garrett, C. J. R., and E. Kunze, 2007: Internal tide generation in the deep ocean. *Annu. Rev. Fluid Mech.*, **39**, 57–87.

Grimshaw, R. H. J., and K. R. Helfrich, 2012: The effect of rotation on internal solitary waves. *IMA J. Appl. Math.*, **77**, 326–339.

Helfrich, K. R., and R. H. J. Grimshaw, 2008: Nonlinear disintegration of the internal tide. *J. Phys. Oceanogr.*, **38**, 686–701.

Helfrich, K. R., and W. K. Melville, 2006: Long nonlinear internal waves. *Annu. Rev. Fluid Mech.*, **38**, 395–425.

Johnston, T. M. S., D. L. Rudnick, M. H. Alford, A. Pickering, and H. L. Simmons, 2013: Internal tidal energy fluxes in the South China Sea from density and velocity measurements by gliders. *J. Geophys. Res.*, **118**, 3939–3949.

Klymak, J. M., R. Pinkel, C. T. Liu, A. K. Liu, and L. David, 2006: Prototypical solitons in the South China Sea. *Geophys. Res. Lett.*, **33 (11)**, L11 607.

Li, Q., D. M. Farmer, T. Duda, and S. Ramp, 2009: Acoustical measurement of nonlinear internal waves using the Inverted Echo Sounder. *J. Atmos. Oceanic Technol.*, **26**, 2228–2242.

Martin, J. P., D. L. Rudnick, and R. Pinkel, 2006: Spatially broad observations of internal waves in the upper ocean at the Hawaiian Ridge. *J. Phys. Oceanogr.*, **36**, 1085–1103.

Ostrovsky, L. A., and Y. A. Stepanyants, 1989: Do internal solitons exist in the ocean? *Rev. Geophys.*, **27**, 293–310.

Pétrélis, F., S. L. Smith, and W. R. Young, 2006: Tidal conversion at a submarine ridge. *J. Phys. Oceanogr.*, **36**, 1053–1071.

Rudnick, D. L., and Coauthors, 2003: From tides to mixing along the Hawaiian ridge. *Science*, **301 (5631)**, 355–357.

Simmons, H., M.-H. Chang, Y.-T. Chang, S.-Y. Chao, O. Fringer, C. R. Jackson, and D. S. Ko, 2011: Modeling and prediction of internal waves in the South China Sea. *Oceanography*, **24**, 88–99.

Subich, C., K. Lamb, and M. Stastna, 2013: Simulation of the Navier–Stokes equations in three dimensions with a spectral collocation method. *Intl. J. Num. Meth. Fluids*, **73**, 103–129.

Sutherland, B. R., 2016: Excitation of superharmonics by internal modes in non-uniformly stratified fluid. *J. Fluid Mech.*, **793**, 335–352.

Sutherland, B. R., and M. S. Dhaliwal, 2022: The nonlinear evolution of internal tides. Part 1: The superharmonic cascade. *J. Fluid Mech.*, **948**, A21.

Vic, C., and Coauthors, 2019: Deep-ocean mixing driven by small-scale internal tides. *Nature Comm.*, **10**, 2099.

Zhang, Z., O. B. Fringer, and S. R. Ramp, 2011: Three-dimensional, nonhydrostatic numerical simulation of nonlinear internal wave generation and propagation in the South China Sea. *J. Geophys. Res.*, **116**, C05 022.